In situ Probing of the Active Site Geometry of Ultrathin Nanowires for the Oxygen Reduction Reaction

Haiqing Liu,[1] Wei An,[2] Yuanyuan Li,[3] Anatoly I. Frenkel,[3] Kotaro Sasaki,[2] Christopher Koenigsmann,[1] Dong Su,[4] Rachel M. Anderson,[5] Richard M. Crooks,[5] Radoslav R. Adzic,[2] Ping Liu,[2] and Stanislaus S. Wong[1,6,*]

[1]Department of Chemistry, State University of New York at Stony Brook, Stony Brook, New York 11794-3400

[2]Chemistry Department, Building 555, Brookhaven National Laboratory, Upton, New York 11973

[3]Department of Physics, Yeshiva University, New York, NY 10016

[4]Center for Functional Nanomaterials, Building 735, Brookhaven National Laboratory, Upton, New York 11973, USA

[5]Department of Chemistry, The University of Texas at Austin, Austin, TX 78712-1224

[6]Condensed Matter Physics and Materials Science Department, Building 480, Brookhaven National Laboratory, Upton, New York 11973

[*]To whom correspondence should be addressed.

Email: sswong@bnl.gov, stanislaus.wong@stonybrook.edu

Keywords: density functional theory; X-ray absorption spectroscopy; ultrathin nanowires; oxygen reduction reaction; surface segregation

Abstract

To create truly effective electrocatalysts for the cathodic reaction governing proton exchange membrane fuel cells (PEMFC), namely the oxygen reduction reaction (ORR), necessitates an accurate and detailed structural understanding of these electrocatalysts, especially at the nanoscale, and to precisely correlate that structure with demonstrable performance enhancement. To address this key issue, we have combined and interwoven theoretical calculations with experimental, spectroscopic observations in order to acquire useful structural insights into the active site geometry with implications for designing optimized nanoscale electrocatalysts with rationally predicted properties. Specifically, we have probed ultrathin (~2 nm) core-shell Pt~Pd_9Au nanowires, which has been previously shown to be excellent candidates for ORR in terms of both activity and long-term stability, from the complementary perspectives of both DFT calculations and X-ray Absorption Spectroscopy (XAS). The combination and correlation of data from both experimental and theoretical studies has revealed for the first time that the catalytically active structure of our ternary nanowires can actually be ascribed to PtAu~Pd possessing a PtAu binary shell and a pure inner Pd core. Moreover, we have plausibly attributed the resulting structure to a specific synthesis step, namely the Cu underpotential deposition (UPD) followed by galvanic replacement with Pt. Hence, the fundamental insights gained into the performance of our ultrathin nanowires from our demonstrated approach will likely guide future directed efforts aimed at broadly improving upon the durability and stability of nanoscale electrocatalysts in general.

1. Introduction

Platinum is known to be the most active catalyst governing the cathodic reaction, namely the oxygen reduction reaction (ORR), in polymer electrolyte membrane fuel cells (PEMFCs) and related direct methanol fuel cells (DMFCs). However, the performance and ubiquity of state-of-the-art Pt-based DMFC anode electrocatalysts, as an example, are limited by issues associated with their relative scarcity, high cost, as well as with their relatively poor performance due to issues associated with high overpotential and slow reaction kinetics. Moreover, these materials can be easily contaminated by oxygen-containing carbon species, such as CO.[1,2]

Therefore, many studies have sought to develop viable alternative architectures in order to improve upon the performance of conventional zero-dimensional (0-D) Pt nanoparticles.[3] Not surprisingly, these efforts have culminated in the rational design and generation of motifs such as but not limited to Pt-metal core-shell materials, ternary alloys, as well as hierarchical ternary or quaternary core-shell structures, so as to reduce the overall usage of Pt.[1,4-12] Our group has focused quite generally on the development of one-dimensional (1-D) core-shell materials, which specifically offer a number of primary benefits toward enhancing the intrinsic activity of electrocatalysts. *First*, crystalline 1-D nanostructures possess (a) high aspect ratios, (b) fewer lattice boundaries, (c) long segments of smooth crystal planes, and (d) a relatively low number of surface defect sites, all of which are desirable attributes for fuel cell catalysts.[13-17] *Second*, we take advantage of the so-called 'ligand effect', induced by the dopant metal upon the overall catalytic performance, in which the transition metal 'M' core will couple with the external Pt shell, thereby resulting in a beneficial coupled electronic and structural effect, which should

facilitate charge transfer and increase reaction kinetics. *Third*, core-shell motifs optimize the use of Pt, thus minimizing Pt loading, and allow for every surface Pt atom to be catalytically accessible. *Fourth*, the addition of the transition metal 'M' will lower the energy of the Pt *d*-band and create *d*-band vacancies, thereby enabling a lowered binding energy of oxygen-containing species,[18] which in turn facilitates the completion of ORR.

More specifically, our group has been probing the effect of systematic variations in size as well as chemical composition in various types of Pt-based 1-D catalysts.[19-23] In terms of trends, we noted that as the nanowire diameter decreases, the corresponding ORR performance increases dramatically, presumably due to lattice contraction of surface atoms originating from surface strain effects.[24,25] Furthermore, our group examined the composition and size-dependent performance in $Pd_{1-x}Au_x$ nanowires (NWs) encapsulated with a conformal Pt monolayer shell ($Pt\sim Pd_{1-x}Au_x$). We noted a volcano-type composition-dependence in the ORR activity of ultrathin $Pt\sim Pd_{1-x}Au_x$ NWs as the Au content was increased from 0 to 30% with the activity of the $Pt\sim Pd_9Au$ NWs (i.e. 0.98 mA/cm^2, 2.54 A/mg_{Pt}, measured at 0.9 V vs. RHE), representing the optimum performance.[21] Although significant enhancements in ORR activity were observed as a function of NW composition, the precise origin of the enhanced performance as a function of NW composition and size remains unclear, since these variables can yield complex and often unforeseen effects on the electronic and structural properties of the analyzed nanostructures and the corresponding catalytic performance.

As a logical extension of that prior finding, in this current report, we probe the intimate physical and electronic structure of these 'optimized' $Pt\sim Pd_{1-x}Au_x$ core-shell type nanostructures used as the starting point with the objective of deducing the nature of

the accompanying catalytic interface therein. Synchrotron X-ray absorption spectroscopy (XAS)-based techniques represent an exciting platform with which to examine the nature of the electronic properties and bonding of 1D catalysts under standard operating electrochemical conditions.[26-29] Extended X-ray absorption fine structure (EXAFS) spectroscopy is known to be as valuable if not superior to other conventional structural analysis techniques, such as TEM or XRD, for obtaining relevant structural information for small, catalytically relevant particles of less than 5 nm.[30-35] Indeed, by analyzing the EXAFS spectrum of each metal within the context of either binary or ternary metallic nanomaterials, information about local structural parameters (i.e. metal-metal coordination number, bond length, and the extent of disorder) can be obtained.[30,36-43] By tuning the X-ray energy to the absorbing edge of each metal, the local environment surrounding atoms of each resonant element can be separately analyzed and compared. For instance, EXAFS has been utilized in not only verifying chemical composition but also probing the detailed formation mechanism of ultrathin Pd-Au alloy nanowires, fabricated through galvanic displacement.[44]

Therefore, the novelty and significance of this current study is that we have not only utilized EXAFS to (i) compare and (ii) differentiate amongst different plausible structural models (i.e. the presence of islands, partial monolayers, or localized alloys) of our as-synthesized Pt~Pd_9Au ultrathin core-shell nanowires under *in situ* electrochemical conditions but also corroborated these data with the net results of well-designed DFT-based computational models. Therefore, the judicious combination and subsequent correlation of data from both experimental and theoretical studies has revealed for the first time that the catalytically active structure of our ternary nanowires can actually be

ascribed to PtAu~Pd possessing a PtAu outer binary shell and a pure inner Pd core. Moreover, we have plausibly attributed the resulting structure to a specific synthesis step, namely the Cu underpotential deposition (UPD) followed by galvanic replacement with Pt. Hence, it is likely that the fundamental insights gained into the performance of our 1-D electrocatalysts using these complementary tools will likely guide future research in terms of defining new directions for substantially improving upon durability and stability.

2. Experimental

2.1. Computational

DFT calculations were performed by using the Vienna *ab initio* simulation package (VASP).[45,46] The spin-restricted GGA-PW91 functional,[47] a plane-wave basis set with an energy cutoff of 400 eV, and the projector augmented wave (PAW) method[48] were adopted. The Brillouin zone of the supercell was sampled by 1×1×5 k-points using the Monkhorst–Pack scheme.[49] The conjugate gradient algorithm was used in optimization, allowing for the convergence of 10^{-4} eV in total energy and 0.02 eV/Å in the Hellmann-Feynman force on each atom.

To model nanowires (NW) using DFT, we constructed cylinder-like $Pd_{1-x}Au_x$@Pt core-shell NWs measuring 2.2 nm in diameter, based upon the experimental observations,[21,23,50] showing that the (111) and (200) surfaces were the dominant facets. Three different chemical compositions of the PdAu core were considered, namely Pd_9Au, Pd_8Au_2, and Pd_7Au_3, which we associated with the experimentally measured lattice parameters of 3.923 Å, 3.934 Å, and 3.948 Å, respectively, and which helped to define the periodic boundary conditions along the wire direction. Two unit cells along the wire

direction were included in a cubic supercell whose size was sufficiently large enough that the separation between the NW sidewalls and their images in the other two directions was >15.0 Å. Furthermore, Pd@Pt and Pt NWs possessing the same size and shape were also included by means of comparison.

The relative stability of various core-shell nanowires (NW) was evaluated using the formation energy in eV/atom, which is defined in Equation 1 as:

$$E_{Form} = [E(NW) - j_{Pt}E(Pt) - m_{Pd}E(Pd) - n_{Au}E(Au)]/(j_{Pt} + m_{Pd} + n_{Au}) \quad [1]$$

where E(NW), E(Pt), E(Pd), and E(Au) represent total energy of the NW, gas-phase Pt, Pd, and Au atom, respectively, while j_{Pt}, m_{Pd}, and n_{Au} designate the number of Pt, Pd, and Au atoms in the NW.

Atomic O was used as a probing adsorbate for the ORR activity. The O-binding energy (denoted as BE-O) has been used as a good "descriptor" for probing the ORR,[51] where the calculated BE-O was correlated with theoretically predicted and experimentally measured ORR activity.[52,53] BE-O is defined in Equation 2 as:

$$BE\text{-}O = E(O/NW) - E(H_2O) + E(H_2) - E(NW) \quad [2]$$

where E(O/NW), $E(H_2O)$, and $E(H_2)$ correspond to the total energy of O-adsorbed NW, water, and hydrogen in the gas phase, respectively. Hence, a more positive BE-O implies weaker O-binding. To calculate BE-O, we chose *fcc* and *hcp* 3-fold hollow sites on (111) terraces far away and nearly equidistant away from the edge, as the (111) terraces of a nanoparticle were found to contribute the most to the observed ORR.[54,55] No geometric constraints were applied during the optimization process, which was found to be essential in order to explicitly capture the subtle and actual size- and shape-effect of real nanocatalysts.[56]

2.2. Synthesis of carbon supported Pd_9Au ultrathin nanowires

Ultrathin Pd-Au nanowires have been prepared, utilizing a method that has been adopted by our group but has been modified to efficiently produce gram-scale quantities of catalyst.[21] Briefly, in a typical experiment, palladium nitrate (0.0504 mmol, 11.7 mg, Alfa Aesar 99.9%), tetrachloroauric acid hydrate (0.0056 mmol, 1.7 mg, $HAuCl_4 \cdot x\ H_2O$, Alfa Aesar, 99.999%), octadecylamine (400 mg, Acros Organics 90%), and dodecyltrimethylammonium bromide (60 mg, TCI >99%) were dissolved in 7 mL of toluene under vigorous magnetic stirring. The entire mixture was left to react under an argon atmosphere, utilizing standard air-sensitive Schlenk-line procedures, and was subsequently sonicated for 20 minutes. Separately, solid sodium borohydride (13 mg, Alfa Aesar 98%) was dissolved into 2 mL of deoxygenated distilled water, and the solution was added dropwise into the precursor mixture, while stirring.

After 1 h of reaction, the mixture was diluted with 2 mL aliquots of distilled water and chloroform, thereby resulting in the separation of the organic and aqueous phases. The black organic phase was then isolated, diluted with 10 mL of absolute ethanol, and eventually centrifuged for 10 min, ultimately resulting in the precipitation of a black solid. The black solid was subsequently washed several times with ethanol, and allowed to dry in air. Adsorption of these as-prepared nanowires onto a conductive carbon support (Vulcan XC-72, Cabot) was achieved by first dispersing the isolated black solid, containing a mixture of Pd nanowires and residual surfactant into 6 mL of chloroform, until a homogeneous black mixture was formed. An equal mass of Vulcan carbon (i.e. ~6 mg) was then added to this mixture, and this was subsequently sonicated for 30 min in a bath sonicator. As-prepared composites were then isolated by centrifugation, and fixed

onto the carbon substrate by immersion in hexanes for 12 h. Multiple successive reactions were performed; accumulated products were isolated in order to achieve a sufficiently large quantity for EXAFS experiments.

2.3. Synthesis of Pt~Pd_9Au core-shell ultrathin nanowires

The preparation of the desired core-shell structure was achieved by utilizing a modified 'bulk' gram-scale synthesis approach, initially reported by Shao et al. We should note that this protocol has never been previously applied to the synthesis of ultrathin nanowires. In effect, the process consists of (a) a UV/ozone treatment followed by (b) CO stripping and (c) Pt deposition. Specifically, Pd_9Au/C was first dispersed into ethanol by sonication after which it was placed onto a watch glass and subsequently dried. The watch glass was placed into a UV ozone generator (UVOCS model no. T10X10-0ES) and treated for 15 min. As-treated nanowires were then isolated from the underlying watch glass by sonication. The 'reactor' environment, where the CO stripping and Pt deposition processes were allowed to occur, consisted of a graphite sheet working electrode, a platinum black (porous Pt film) counter electrode, and an Ag/AgCl (BASi) leak-free reference electrode.

The UV/ozone treated sample was pre-dispersed in 50 mM H_2SO_4, and then added to the 'reactor', prior to the 'CO stripping' step. Adsorption of CO was achieved by bubbling in CO gas into the electrolyte for 30 minutes, thereby forming a CO-saturated solution. Then the adsorbed CO was subsequently stripped from the surface by a potential sweep, running up to 1.1 V at 20 mV/s. After pretreatment, a de-aerated aqueous $CuSO_4$ solution in 50 mM H_2SO_4 was added to the 'reactor' in order to obtain a Cu^{2+} concentration of 50 mM. After addition of $CuSO_4$, the potential was held constant at

approximately 400 mV (vs. RHE) in order to deposit a monolayer of Cu onto the Pd_9Au nanowires. A de-aerated aqueous solution of K_2PtCl_4 in 50 mM H_2SO_4 was immediately added dropwise to the 'reactor' in order to initiate galvanic replacement of the Cu by the Pt. After 5~10 minutes, the reaction was complete. The catalysts were subsequently washed with MilliQ UV-plus water, and centrifuged. The resulting catalyst powder, denoted as Pt~Pd_9Au/C, was dried in vacuum at 80ºC prior to further analysis.

2.4. Materials Characterization

The as-prepared Pt~Pd_9Au nanowires were structurally probed using transmission electron microscopy (TEM). Energy dispersive x-ray analysis (EDS) was performed to obtain relevant data aimed at ascertaining the overall nanowire chemical composition, using a JEOL-1400 TEM instrument. High angle annular darkfield (HAADF) STEM images and electron energy loss spectroscopy (EELS) data were collected using a Hitachi aberration-corrected scanning transmission electron microscope (HD-2700C). Specimens for all of these microscopy experiments were prepared by dispersing the as-prepared product in ethanol, sonicating for 2 min to ensure an adequate dispersion of the nanostructures, and evaporating one drop of the solution onto a 300 mesh Cu grid, coated with a lacey carbon film.

2.5. Electrochemical Setup

The special home-made electrochemical cell[57] we used for our experiments is composed of several Teflon pieces, clamped together to form an electrolyte reservoir, whose maximum inner volume measured around 30 mL. The center of the cell is carved and sealed with Kapton tape to ensure a clear path for the X-ray beam. Other components of the setup include an Ag/AgCl (BASi) leak-free reference electrode and a glassy carbon

counter electrode. As-synthesized Pt~Pd_9Au/C nanowires were deposited onto a piece of carbon paper so as to form a homogeneous layer. Then the carbon paper was placed into the cell as a working electrode. The electrolyte utilized herein was 0.1 M $HClO_4$.

Prior to measurement, oxygen gas was purged through the electrolyte for 10-15 minutes so as to ensure an O_2-saturated solution. For the cycling process which simulated a normal ORR environment, the potential was cycled from 0.6 to 1.0 V. EXAFS measurements and CV spectra were obtained after 0, 10, 50, 250, 500, 750, and 1000 cycles, respectively. EXAFS spectra were collected whilst maintaining an oxygen-free environment by purging Ar throughout the entire process of data collection. The applied potential was held at a relatively low value (i.e., 0.5 V vs. RHE), in order to prevent possible surface oxide formation, which would have resulted in likely complications associated with the fitting of the EXAFS spectra. We note that cyclic voltammetry was performed in a deoxygenated solution (by purging Ar for 10-15 minutes) with a scan rate of 20 mV/s.

2.6. EXAFS

At the National Synchrotron Light Source, both Pt L_3-edge and Au L_3-edge data were collected at the X18A beamline with both sets of measurements obtained in the fluorescence mode. Different parameters contributing to the theoretical EXAFS equation (e.g., bond distances and energy origin correction or coordination numbers and the bond length disorder parameters) correlate into the resulting fit. Constraining them during the fit improves the stability and viability of the results. In our analysis, we modeled the Pt and Au L_3-edge data concurrently by applying multiple constraints.[34] Only Pt-Au and Pt-Pt as well as Au-Pt, Au-Au, and Au-Pd data contributed to the Pt and Au EXAFS results,

respectively. Details of the data analysis and modeling are given in the Supporting Information section.

3. Results and Discussion

3.1. Theoretical calculations

DFT calculations were performed to determine the distribution of Au in our NWs. It is known[58] that Au-metal alloy systems appear to undergo some level of Au surface segregation. This phenomenon is even more apparent and noticeable when either (a) the metal content or particle size is increased or when (b) the temperature is elevated.[59] In our DFT calculations, we first mapped out the adsorption preference of a single Au atom on a Pd NW (Figure 1). Similar to the case of nanoparticles,[60,61] a decreasing sequence was observed: edge (111) / (111) (A, 0.00 eV/atom, Figure 1) > edge (111) / (100) (B, 0.02 eV/atom) > Terrace (100) (C, 0.05 eV/atom) > Terrace (111) (D, 0.09 eV/atom). That is, the more active the Pd on the NW surface, the more energetically favorable it is to be replaced by Au. Moreover, we also noticed that adsorption of oxygen species during the ORR could induce either a surface restructuring or reconstruction process in Pt core-shell nanoparticles, which favored surface segregation of oxophilic core elements;[62] yet for an PtAu system, at least up to 0.25 ML of O was required in vacuum to allow for the segregation of Pt back to the shell.[63]

Accordingly, for a PdAu@Pt NW, we simulated three possible variations in structural configurations in order to obtain details concerning Au distribution within these ultrathin NWs, as shown in Figure 2: (i) $Pd_{(1-x)}Au_x$@Pt NWs with all Au atoms staying within the core; (ii) $Pd_{(1-x)}Au_{(x-y)}Pt_z$@$Au_yPt_{(1-z)}$ NWs with a portion of Au atoms

segregated to the edge of the Pt shell; and (iii) $Pd_{(1-x)}Pt_z@Au_xPt_{(1-z)}$ NWs with all Au atoms segregated to the Pt shell. Herein, (x, y) and z denote the mole ratios of Au/(Au+Pd) and Pt, respectively. $Pd_{(1-x)}Au_x@Pt$ was used to model the as-prepared sample, while $Pd_{(1-x)}Au_{(x-y)}Pt_z@Au_yPt_{(1-z)}$ and $Pd_{(1-x)}Pt_z@Au_xPt_{(1-z)}$ were included in consideration of either partial or full segregation of Au to the shell during the ORR. We arranged Au atoms symmetrically in a way such that Au preferentially replaced the active Pd sites on the surface as demonstrated above, but avoided the formation of Au-Au bonds within the core, according to experiment (Figure 2).[21,23] Such an arrangement was aimed at lowering the total energy of each type of NWs, while making the calculated BE-O comparable among three types of NWs.

It is believed that the electrochemically active sites in our system consist effectively of the outermost surface Pt atoms. Essentially, due to the presence of a filled *d*-band, Au itself is inactive towards ORR.[64] Moreover, it has been demonstrated that Au surfaces do not adsorb oxygen in the relevant potential window for ORR (i.e. ~0.7-1.0V vs. RHE) in acidic media.[65] Therefore, it is reasonable to conclude that the segregated Au atoms are largely non-active for ORR and that they are essentially 'spectators', with respect to the actual catalytic reaction.

Figure 3 highlights the calculated E_{Form} for all NWs studied. When the chemical composition was kept constant, one can see that the as-prepared sample, i.e. $Pd_{(1-x)}Au_x@Pt$ NWs, is the least stable, but that the stability can be gradually increased by either partial, i.e. $Pd_{(1-x)}Au_{(x-y)}Pt_z@Au_yPt_{(1-z)}$, or full, i.e. $Pd_{(1-x)}Pt_z@Au_xPt_{(1-z)}$, segregation of Au to the shell. That is, Au within the core prefers to segregate to the shell and occupy both the active edge sites as well as the (100) terrace sites. This is in line with

the strong tendency of Au atoms to segregate in the host of most metals.[66,67] When varying the composition, the stability of alloy NWs in term of E_{Form} decreases with increasing Au. The maximum of E_{Form} is observed for pure Pt NWs (E_{Form} = -5.27 eV/atom) followed by Pd@Pt (E_{Form} = -4.17 eV/atom), while that associated with Pd@AuPt is -4.14, -4.12, and -4.09 eV/atom, corresponding to Au/(Au+Pd) ratios of 0.1, 0.2, and 0.3, respectively.

At the temperature for the ORR (i.e. below 100°C), the thermal stability of NWs is less critical than their electrochemical stability, because metal catalysts can be oxidized and dissolved into electrolyte. Since Au (1.52 V) possesses a higher reduction potential than both Pt (1.19 V) and Pd (0.92 V), alloying Au into NW structures is expected to contribute to their resistance to oxidation, though their thermal stability can be slightly compromised. This finding agrees well with the experimental observations that Au-alloyed NWs demonstrated a greatly improved electrochemical stability as compared with Pd@Pt NWs.[21,23,50]

To scale the ORR activity, BE-O values were calculated and plotted in Figure 4. According to the previous study,[51] the removal of oxygen-containing species via either protonation or the formation of *O, *OH, or $*O_2$ was found to slow down the ORR on Pt, depending on the precise experimental conditions. Therefore, it is reasonable to assume that a higher BE-O (more positive) should lead to a weaker interaction between Pt atoms and oxygen-containing species, thereby ensuring a greater overall ORR performance.[52,53] Of course, an excessive weakening of O-binding will hinder the ORR, wherein the adsorption of oxygen-containing species becomes problematic. One can see that Pd@Pt NWs (BE-O = 1.46 eV at the *fc*c site and 1.76 eV at the *hcp* site) can bind oxygen more

weakly than Pt NWs (BE-O = 1.44 eV at the *fcc* site and 1.82 eV at the *hcp* site). The effect of adding Au on BE-O depends on the spatial distribution of Au, while BE-O is not necessarily sensitive to variation in the amount of Au.

In the case of Au with an Au/(Au+Pd) ratio of 0.12 for instance, the BE-O for Pd@Pt is decreased by 0.2 ~ 0.3 eV when adding Au into the Pd core (Figure 4i), while it is decreased by 0.1 ~ 0.2 eV (Figure 4ii) and increased by 0.1 ~ 0.2 eV (Figure 4iii) by partial and full segregation of these Au atoms from the core to the shell, respectively. By comparison, we note that the corresponding variation in BE-O values for AuPd@Pt NWs as a function of the Au/(Au+Pd) ratio is smaller (within 0.1 eV), when the same spatial distribution of Au is analyzed.

The variation trend in BE-O correlates well with the surface strain before oxygen adsorption, $S_{Pt\text{-}Pt}= [d_{Pt\text{-}Pt}(NW)/d_{Pt\text{-}Pt}(Pt\ bulk) – 1] \times 100$ (Figure 5). Herein, only the active (111) terrace of either the Pt shell or the Pt(111) shell was considered. The lattice constants used herein for Pt, Pd, and Au, respectively, are 3.924 Å, 3.890 Å and 4.080 Å. As compared with Pt bulk, the formation of NWs introduces significant surface contraction on the Pt(111) shell (i.e. $S_{Pt\text{-}Pt} = -2.2$ %, displayed as dots in Figure 5a). Due to the similar lattice between Pt and Pd, using Pd as the core only leads to small changes in the surface strain and therefore, the BE-O value. Adding Au into the core, thereby forming a PdAu alloy, diminishes the perturbative effect of contraction, and therefore, BE-O is lowered (square, Figure 5a), in agreement with a previous study.[68] In principle, the more Au is added into the core, the lower the surface strain will be, and therefore, the more strongly the oxygen will be bound. The caveat is that at high Au concentrations, the nanowire surface not only adopts a tensile strain but also can be fully covered by Au sites

due to the segregation, all of which can potentially inhibit ORR activity.

With all Au segregated into the shell, the Pt(111) shell becomes more contracted as compared with Pt NWs, i.e. from 0.1% to 0.6% with increasing amounts of Au (triangles, Figure 5a). However, the corresponding BE-O therefore stays more or less around 1.55 eV. This value is associated with the local structural flexibility of NWs. The variation in the BE-O values as a function of $S_{Pt\text{-}Pt}$ prior to oxygen adsorption (Figure 5a) can be compared and correlated with that of $S_{Pt\text{-}Pt}$ after oxygen adsorption as a function of $S_{Pt\text{-}Pt}$ before oxygen adsorption (Figure 5b). For $Pd_{(1-x)}Au_x$@Pt NWs, the relatively small contraction in the Pt(111) shell promotes surface flexibility. With increasing amounts of Au in the core, the adsorption of oxygen can introduce additional surface distortion. It has been demonstrated that lowering the degree of contraction on the neighboring Pt can perceptibly introduce tensile strain with $S_{Pt\text{-}Pt}$ values, ranging from 5.5% to 6.5%. As a result, the Pt-O interaction is strengthened (Figure 5a). By contrast, for $Pd_{(1-x)}Pt_z$@$Au_xPt_{(1-z)}$ NWs, the strong degree of contraction renders the NW more rigid. Hence, the response to oxygen adsorption is much less ($S_{Pt\text{-}Pt} < 4.6\%$, Figure 5b) and the variation in $S_{Pt\text{-}Pt}$ with the amount of Au in the shell is less significant. As a result, BE-O is more positive and is not sensitive to the amount of Au in the shell (Figure 5a).

Our results indicate that the distribution of Au plays an important role in tuning the surface strain of AuPd@Pt NWs and therefore of BE-O. In particular, the segregation of Au to the shell implies two specific consequences: (1) it is able to stabilize the NWs (Figure 3), and (2) it increases the rigidity of the NW, which prevents the structural distortion upon oxygen adsorption and thereby weakens the binding energy (Figure 4).

The importance of structural rigidity in influencing the observed oxygen binding

energy has been highlighted in our previous theoretical analysis of ORR on Pt@Pd nanoparticles, possessing a tetrahedral shape.[56] Specifically, we determined in that prior work that for nanostructures with a relatively significant surface contraction, i.e. such as the ~2.3% noted for the PdAu@Pt NWs studied herein, the presence of oxygen adsorption can thereby lead to a more significant distortion of the localized structure of the (111) facet as compared with the corresponding (111) bulk surface. That is, nanostructures are intrinsically more flexible in their local structure as compared with bulk surfaces. This surface distortion which accommodates for the adsorption of oxygen can thereby lead to an increased binding energy of oxygen. It is noteworthy that the correlation between the metal *d*-band structure before adsorption and the oxygen binding energy, which is often used to explain the trend in binding energy on metal surfaces, does not necessarily apply for such nanostructures, since the resulting *d*-band structure of distorted metal sites at the nanoscale limit can be very different after oxygen adsorption.

Hence, the rigidity of the local structure plays a more important role. That is, for the same kind of adsorption site, the more flexible the structure is, the more easily the interacted metal atoms can distort upon adsorption, all of which can thereby lead to a stronger oxygen binding. Indeed, only when the NW adopts the conformation of $Pd_{(1-x)}Pt_z@Au_xPt_{(1-z)}$ does the BE-O of AuPd@Pt NW become weaker than that of Pd@Pt (Figure 5(iii)). Therefore, a higher ORR activity is expected. However, the degree of weakening is small, and hence, it is difficult to draw any clear and unequivocal conclusions that would correlate exactly with the experimentally measured ORR activity values, obtained by simply examining the trends in BE-O.[21,23,50]

Considering the gap between the BE-O and the ORR activity, we have taken on

the additional step of estimating the mass and specific ORR activity values, based on the calculated BE-Os. Considering that the promotion of ORR activity on Pt was predicted by weakening the Pt-O bond,[51] we have estimated the mass activity as $\Delta A_M \propto \exp(-0.5*BE\text{-}O/k_bT)*N_{Pt}(111)/N_{Pt}(total)$, wherein $N_{Pt}(total)$ and $N_{Pt}(111)$ represents the number of Pt atoms in the NWs and on the (111) terrace, respectively. The charge transfer coefficient was chosen as "0.5" on the basis of previous experimental and theoretical studies.[69,70] The specific activity was estimated as $\Delta A_S \propto \exp(-0.5*BE\text{-}O/k_bT)*N_{Pt}(111)/N_{Pt}(shell)$, wherein $N_{Pt}(shell)$ represents the number of Pt atoms in the shell of the NR. The edge and (100) terrace sites, which account for 38% of total Pt surface sites, were assumed to be inactive and not involved in the ORR process.

Figure 6 plots the variation of relative activity at T = 20°C, i.e. mass activity and specific activity, with respect to Pt NWs. We first want to clarify that all the activities reported here correspond to a potential of 0.9 V (vs. RHE), unless otherwise specified. We note that both mass and specific activities for pure Pt NWs are set to 1 in the following Figures. A significant variation of ORR activity with respect to both the amount and distribution of Au within the AuPd@Pt NWs was observed. For a NW with a certain quantity of Au, $Pd_{(1-x)}Pt_z@Au_xPt_{(1-z)}$ NWs possessing full segregation of Au within the shell (panels E and F) displayed the largest improvements in both mass and specific activities with respect to pure Pt NWs amongst all three types of NWs we studied. By comparison, the ORR activities of $Pd_{(1-x)}Au_{(x-y)}Pt_z@Au_yPt_{(1-z)}$ NWs with partial Au segregation (panels C and D) and of as-prepared $Pd_{(1-x)}Au_x$@Pt NWs with Au localized in the core (panels A and B) are far lower. That is, the small variation in BE-O obtained by alloying Au (Figure 5a) can have a dramatic effect upon the ORR activity.

For a certain Au distribution, the observed enhancements of both mass and specific activities do depend on the amount of Au. Specifically, the experimentally observed trend in both types of activities in evolving from Pt and Pd@Pt to Au-containing analogues such as Pd_9Au@Pt, Pd_8Au_2@Pt, and Pd_7Au_3@Pt [21] can be well captured and described by the corresponding trend in the theoretically estimated activity only when the $Pd_{(1-x)}Pt_z@Au_xPt_{(1-z)}$ conformation is adopted and analyzed. A direct comparison between the "volcano" trend observed in our theoretical estimations and that found in our corresponding experimental data is shown in Figure 7. It is worth emphasizing that both sets of data point to Pd_9Au@Pt as the optimal chemical composition of the cathode for the ORR.[21] According to our DFT calculations, either the partial or full segregation of Au is best able to stabilize the as-prepared $Pd_{(1-x)}Au_x$@Pt NWs, which is likely to occur during the ORR process, whereas the structures of other types of as-prepared NWs may not be able to capture the behavior of the catalyst under operational ORR conditions.

Overall, our DFT calculations show that the ORR activity of AuPd@Pt NWs can be well tuned by purposefully varying the amount and distribution of Au. In effect, the segregation of Au from the core to the edge and (100) terrace sites of the shell is likely to occur during the ORR process and can promote the ORR activity significantly. We note that the more Au remains in the core, the lower the ORR activity of the corresponding AuPd@Pt NW. In addition, the amount of Au should be moderate, i.e. large enough in order to render the NW rigid and therefore weaken the O-Pt interaction, while small enough to prevent both the decrease of active Pt sites in the shell as well as the overall confinement of Au to the core.

In essence, our theoretical computations have attributed the possibility of this hierarchical architecture as emanating from the *in situ* machinations of the oxygen reduction reaction process, thereby resulting in the dynamic surface segregation of certain metal elements within Pt-outer shell, metal/metal alloy core nanoparticles. However, because prior experimental reports have been effectively bulk measurements, these have neither specifically established nor determined the validity of this hypothesis. Hence, in order to better understand and verify the plausible localized restructuring within our Pt~PdAu ultrathin nanowire systems, we have collected EXAFS data.

3.2. Experimentally probing core-shell nanowires with STEM, EELS, and EXAFS

We have previously reported on the synthesis of as-prepared homogeneous Pd_9Au ultrathin nanowires, which represent the precursor to the focal core-shell structure of this study.[62] According to the structural characterization results obtained from both X-ray diffraction (XRD) and TEM-based selected area electron diffraction (SAED), the measured lattice *d*-spacings in the as-prepared series of $Pd_{1-x}Au_x$ nanowires match perfectly with the predicted values calculated based on the overall chemical composition, thereby verifying the existence of a homogeneous alloy-type material as opposed to either a core-shell or even a partial alloy motif.

To justify the choice of this very particular nanoscale system for such an elaborate study, we have provided a detailed rationale, based on previous theoretical and experimental results. Specifically, according to the "volcano" plot put forth by Nørskov et al., the challenge for optimizing Pt-based electrocatalysts for ORR has mainly been to overcome the fact that the adsorption energy of oxygen onto Pt is very strong.[51] Hence, in Pt-Pd core-shell structures in particular, the outer Pd atoms not only act as a support but

also contribute to the tuning of the electronic properties of the underlying Pt atoms.[71] However, the presence of a Pt monolayer on a bare Pd substrate may not necessarily represent the optimal structural motif. As discussed in the manuscript, the lattice constants of Pt, Pd, and Au are 3.924, 3.890, and 4.080 Å, respectively. Therefore, when deposited onto either bare Pd or Au, the Pt monolayer may experience either a compressive or a tensile strain, respectively, thereby potentially altering the observed Pt-Pt interatomic distances. Prior reports have demonstrated that the ideal Pt-Pt distance can be achieved by utilizing as the underlying 'substrate', Pd-Au alloy nanoparticles possessing a Pd: Au molar ratio, that is close to 9:1.[72] This supposition has actually been validated previously in our work with analogous ultrathin nanowire system.[21]

Hence, in this paper, we chose our most active ORR sample, namely Pd_9Au, as the 'foundational' model material with which to pursue our subsequent studies. Upon deposition of Pt, the morphology and chemical composition of as-prepared carbon-supported Pt~Pd_9Au nanowires were characterized by electron microscopy, as shown in Figure 8. Specifically, we noted that as-generated Pt~Pd_9Au ultrathin nanowires gave rise to an interconnected network morphology, with average diameters of individual wires measuring 2.5 ± 0.3 nm. As a consequence of the formation mechanism of the Pd_9Au nanowires, there was a juxtaposition of a small quantity of incompletely grown, short nanorods[73] coupled with a majority of longer nanowires possessing average lengths of several tens of nanometers.

The higher resolution STEM image coupled with the cross-sectional EELS analysis indicated that the nanowires most likely possessed a core-shell structure. What is important to note is that with STEM, the Pt and Au elements could not be readily

differentiated as a result of their extremely close and potentially overlapping signature bands. However, it is clear from Figure 8D that both of these two elements were richer in quantity and distribution at the outer, external circumference of the wires as compared with within the inner central core-region. The overall elemental composition derived from EDS analysis was determined to be Pt: Pd: Au = 7: 81: 12, with small uncertainties of roughly 2-3% in terms of the atomic ratio reported. The Pd: Au ratio was very close to the expected ratio of 90: 10 inherent to a Pd_9Au nanowire. Therefore, our Pt~PdAu sample could be actually ascribed to a $Pt_7Pd_{81}Au_{12}$ composition.

Nevertheless, upon the deposition of that Pt outer shell, what has been missing to date has been a precise study and inherent understanding of the actual spatial distribution of all three elements, namely Pt, Pd, and Au, within the nominal Pt~PdAu core-shell motif in order to fully corroborate our computational findings. Indeed, we ourselves have previously shown[21] that even though there is a systematic trend in the oxide reduction peaks in cyclic voltammograms (CV) for the series of $Pd_{1-x}Au_x$ nanowires as a function of varying "x" values, as we proceeded to deposit an outer Pt monolayer, the aforementioned trend in CVs becomes much less defined and could therefore not serve as a means of precisely examining surface stoichiometry. We hypothesize that this is due to the fact the surface is now almost exclusively covered by Pt atoms whose electronic structure is only slightly modified by the underlying PdAu core giving rise to a subtle if almost imperceptible alteration in the accompanying CV profiles.[21]

As a means of overcoming these inherent sensitivity limitations as discussed in the Introduction, EXAFS is known as an excellent tool for probing the local atomic environment within both bulk and nanomaterial systems. Therefore, we conducted a

series of time-dependent *in situ* EXAFS experiments which enabled us to examine the effect of the ORR reaction on possible restructuring of our core-shell Pt~PdAu nanowires, since we assert that surface catalysis of O_2 species lies at the origin of our observed structural modification. Specifically, we deposited Pt~Pd_9Au nanowires onto conductive carbon paper, which was then placed into an electrochemical cell, which had been specially designed for XAFS experiments. By doing so, we were able to perform the oxygen reduction reaction on our catalysts while obtaining spectra at designated time points of interest, as the reaction systematically progressed in a range spanning 0 to 1000 cycles. It should be noted at the outset that the EXAFS data support all of our previous complementary spectroscopy and microscopy data indicating the formation of a core-shell motif.

In terms of actual EXAFS data, since Pt and Au atoms are similar in terms of their X-ray scattering properties, it was nearly impossible to distinguish between these two types of atoms as neighbors to either Pt or Au. Hence they are considered as equivalent in the fit. The relevant analysis details of each individual spectrum can be found in the Supporting Information section (Figure S1 and S2). A summary of as-obtained structural parameters, including coordination numbers, bond lengths, and their mean square disorders, is displayed in Tables 1 and 2.

From these collected data, we should note that the atomic ratio of Au: Pt can be directly calculated from the edge step of their respective regions within the EXAFS spectra. The corresponding data are displayed in Figure S3. As a result, the Au: Pt ratio was computed to be 2.5 ± 0.2, whereas the analogous ratio value derived from EDAX data was 1.7 ± 0.7. We should clarify that both Au and Pt elements constitute a minority

composition of the overall core-shell Pt~Pd_9Au structure (i.e. close to 10%), thereby leading to a relatively large error (i.e. 2~3%) associated with the actual experimental percentage values themselves, i.e. 7% for Pt and 12% for Au, respectively, for our reported values. Therefore, it is reasonable to assume that the experimental ratios derived from EDAX and EXAFS, respectively, would be significantly different. Nonetheless, we noted that in fact, the two sets of data are comparatively close to each other in magnitude, thereby confirming the validity and reliability of the Pt: Pd: Au = 7: 81: 12 EDAX composition ratio we had noted earlier in the paper.

When the Pt L_3 edge was analyzed, the coordination number of the first nearest neighboring Pt-Au/Pt was determined to be 9-10, suggesting that the Pt atoms herein are predominantly surrounded by either Pt or Au atoms. According to the chemical composition determined by EDS analysis, the sum of Pt and Au was less than 20% in terms of atomic ratio. In other words, if Pt atoms were to form a random alloy with the two other elements, it is very likely that this occurred with Pd atoms, since Pd constitutes the majority of the wire composition, as opposed to either Pt or Au. Such a conclusion suggests that Pt atoms are essentially exclusively localized on the surfaces of the nanowires themselves. In effect, the EXAFS and EELS data have collectively suggested that as a result of the Cu underpotential deposition (UPD) process followed by galvanic replacement with Pt, the resulting core-shell structure likely possesses a thin outer Pt shell as opposed to a more randomized inner Pt-metal alloy.

Regarding the Au L_3 edge, the results are far more novel and intriguing. Specifically, the coordination numbers for both Au-Au/Pt and Au-Pd are quite close to 6, with a reasonably small error bar. In essence, this implies that every Au atom is

surrounded by 6 Pd atoms and either 6 Pt or Au atoms. From the known actual chemical composition of Pt_7~$Pd_{81}Au_{12}$, as determined from EDS, such a conclusion is inconsistent with a picture in which Au atoms are mixing homogeneously with Pd atoms within the core. The latter model would envision Au to be almost exclusively surrounded by Pd atoms, because Pt was found (vide supra) to be localized on the surface of the nanowires.

Since from the Pt L_3 edge data, we know that Pt is exclusively localized on the surface, we can only deduce that the Au atoms either are immediately beneath this uppermost layer forming a "sublayer" or are well mixed with the Pt layer itself, thereby creating a PtAu-shell / Pd-core structure. A clear differentiation between these two plausible structural scenarios is beyond the scope of this particular work and would require a clear and obvious differentiation between signals attributed to Pt and Au atoms, respectively, in the EXAFS data, which is difficult to accomplish. Notwithstanding, our results clearly show that Au atoms are not randomly distributed within the Pd_9Au nanowires and most likely have undergone some degree of surface segregation.

Herein, we should note that consideration of oxygenated Pt, such as Pt-OH_2, Pt-OH, and Pt-O, has been excluded from the fitting process. Nonetheless, the resulting simulated data matched perfectly well with experimental curves which thereby implies that the presence of a range of Pt-O species gives rise to extremely minor, if any perceptible, influence on the EXAFS spectra. In other words, the amount of surface oxide species present, such as Pt-OH_2, Pt-OH, or Pt-O, was likely to be scarce, and coverage is expected to be low. Such an assertion is reasonable, since we have purposely minimized the potential for surface oxidation (i) through Ar purging as well as (ii) by holding the

potential within a “reducing” region, i.e. 0.5 V vs. RHE in this case, during spectra collection, as mentioned in the Experimental Section.

Also, it is important to note that we have periodically collected cyclic voltammograms of the sample in between our EXAFS measurements, as shown in Figure S4. Overall, there are relatively insignificant differences in the CVs obtained throughout the course of the entire experiment, namely throughout 1000 ORR cycles. Minor changes we have discerned include (a) a slight reduction in the hydrogen adsorption/desorption ($H_{ads/des}$) peaks as well as (b) a subtle fluctuation of the oxide reduction peak position. Nevertheless, both of these observations have been previously detected in our Pt~Pd ultrathin nanowires, while conducting a similar time-resolved ORR experiment.[20] More importantly, in that system, these slight variations in CVs barely affected either the corresponding ORR performance or the final morphology observed.

Moreover, to back up existing data, we also examined the morphology and chemical composition of the sample after ORR treatment, as shown in Figure S5. Even though we noted a certain degree of aggregation of the nanowires themselves, it was evident that the structural integrity of the individual wires themselves was mostly preserved. Furthermore, we obtained a chemical composition of $Pt_9Pd_{79}Au_{12}$ for the wires after electrochemical processing; these data were obtained by performing localized EDAX analysis, and were very similar to what had been observed prior to the electrochemical experiments, i.e. $Pt_7Pd_{81}Au_{12}$. Therefore, we can conclude that during the entire time-dependent EXAFS experiment, the sample remained relatively unchanged in terms of both morphology and electrochemical performance.

Regarding the origin of the stability of these novel nanostructures, the presence of both the Pt monolayer and Au sub-layer contribute to the enhancement of stability of our resulting ternary core-shell structure. *First*, it is plausible that the presence of a Pt monolayer, as opposed to relatively "bulky" Pt, such as elemental Pt nanoparticles, induces an enhanced catalytic stability, as it can decrease the oxidation of the Pt, that may occur from interaction with the underlying alloyed substrate. This behavior has been readily noted in PtRu systems, and can be readily generalized to many other Pt-M binary electrocatalysts.[74] *Second*, the addition of Au atoms can render the surface to be more 'noble'. Specifically, we have shown in the past that the oxide reduction peak of the Pd_9Au NWs can be shifted by 20 mV to higher potentials as compared with bare Pd NWs.[21] This result highlighted that Pd_9Au NWs gave rise to weaker interactions with the adsorbed oxygen species, thereby implying a potential enhancement against possible surface corrosion in acidic media. Furthermore, according to conclusions drawn from our EXAFS results, it is reasonable to affirm that the Au atoms had segregated onto the surface, thereby resulting in an Au-rich sublayer in the final structure.

Moreover, a similar type of hierarchical structure, namely incorporating a Ni@Au@PtNi core-interlayer-shell, has been designed by Kang et al., wherein the presence of an Au interlayer was found to have effectively inhibited surface oxide formation, thereby improving the overall long-term durability.[75] These observations and examples support our motivation for incorporating Au into our nanowire system.

To further confirm and corroborate the observed surface segregation within our hierarchical nanowires, we also conducted EXAFS experiments on so-called "freshly-made" Pt~Pd_9Au samples, prepared as a powder as opposed to being deposited on carbon

paper and immersed into electrolyte. According to Tables 1 and 2, these samples exhibited identical local structure and behavior to the sample that had undergone electrochemical testing. Such consistency in our data implies that the Au surface segregation originated from the intrinsic synthesis and treatment process prior to the exposure of the sample to electrochemical processing, as opposed to the very ORR reaction itself. In other words, by a process of elimination, we propose that the most probable initiator, i.e. instigating event, of the observed surface segregation can be ascribed to Cu underpotential deposition followed by galvanic replacement with Pt.

To justify the validity of our conclusions, it is worth noting that similar types of behavior have been reported in cases where the presence of different absorbates can result in surface segregation in metal alloy systems. Specifically, Pt atoms in Pt_3Co nanoparticles can undergo a surface-segregation during a CO annealing process at 200°C, resulting in the formation of a Pt-shell, PtCo-core structure.[76] Moreover, high-temperature is not a necessary prerequisite for such surface restructuring to occur. For instance, Völker *et al.* have observed room-temperature O_2-induced Cu surface segregation in polycrystalline bulk Cu-Au alloys using time-resolved XPS experiments and rationalized these observations based on DFT calculations.[77] Similarly, Jirkovsky *et al.* discovered a reversible, external potential-dependent exchange process involving Pd, between the core and the shell within Pd-Au alloy (Pd-rich) nanoparticles.[78] In other words, the chemical compositions of the surfaces of these Pd-Au nanoparticles appeared to depend on the magnitude of the applied potential. For example, at low potentials (i.e. below 0.8 V vs. RHE), the surface tended to be Au-rich, whereas at correspondingly higher potentials (i.e. higher than 1.0 V vs. RHE), the surface was found to be Pd-rich.

This latter paper serves as corroboration of our hypothesis, since our entire Cu UPD process described herein was conducted under a potential range of 0.5-0.8 V (vs. RHE). Hence it is reasonable of us to propose Au segregation in the outer shell. Furthermore, it is worth noting that the relevant operating ORR potential is merely within the 0.6-1.0 V range, which might not be sufficiently high enough to initiate the generation of an alternative scenario, i.e. a Pd-rich surface.

4. Conclusions

In this work, we have probed the local structure of our Pt~Pd_9Au ultrathin nanowires by a holistic approach consisting of a unique combination of both theoretical calculations as well as X-ray Absorption Fine Structure Spectroscopy (XAFS). Specifically, DFT calculations of the binding energy (BE-O) values of oxygen species coupled with the corresponding calculated ORR activities have allowed us to re-visit our assumed 'Pt-shell, PdAu random-alloy-core' model we had proposed in our previous work as a definitive description of Pt~Pd_xAu_{1-x}. In particular, the time-dependent EXAFS data on our Pt~Pd_9Au nanowires have confirmed that (a) Au atoms will likely undergo surface segregation and that (b) such segregation process likely happens during the synthesis of the core-shell structure itself, i.e., in the midst of the Cu UPD process followed by galvanic replacement with Pt, implying that the 'restructuring' occurs primarily upon polarization.

By contrast with many other studies which have utilized DFT calculations and/or XAFS techniques to probe structural parameters, we have used our DFT results herein as a guide towards thoughtfully designing EXAFS experiments. In other words, theoretical

predictions have directed our experiments as well as simplified the resulting analysis by providing for plausible possible structural models with which to differentiate, discriminate, and ultimately verify using EXAFS. Such a synergetic, feedback-based effort will likely be important and relevant for future applications of XAFS.

Meanwhile, the discovery of structural alterations ascribed to the idiosyncrasies of specific synthesis approaches may lead to new perspectives in terms of understanding the structural basis for electrocatalysis, especially with a host of different and complementary nanoscale Pt-based hierarchical nanomaterials. To our knowledge, this is the first time that Au segregation has been reported as a result of a seemingly unrelated Cu UPD/Pt galvanic displacement process. In the future, it will be worth further differentiating between the specific significance of chemical composition versus that of the ultrathin size in terms of explaining the nature of the phenomena observed.

In summary, the novelty and importance of this report arises from combining disparate, complementary, but nonetheless mutually supportive results from (a) in situ spectroscopy, (b) DFT calculations, and (c) electrochemical data into a comprehensive and substantive analysis for understanding the behavior of functionally relevant nanostructures. Very few analogous reports exist.[37,79,80] From a broader perspective, we wish to emphasize the value and wisdom of this approach for gaining key insights into nanoscale structure-property correlations. In particular, the precise examination of local structure and bonding can facilitate a proper understanding of existing nanomaterials and hence an ability to rationally design truly distinctive classes of nanostructures. Hence, the strategy employed herein can be readily generalized to other classes of materials as well to the study of phenomena that have significance beyond ORR and/or electrochemistry.

5. Acknowledgements

Funds for research work (including support for HQ and SSW) at Brookhaven National Laboratory (BNL) were provided by the U.S. Department of Energy, Office of Basic Energy Sciences, Materials Sciences and Engineering Division under Contract No. DE-AC02-98CH10886 and DE-SC-00112704. AIF acknowledges support from the Department of Energy Grant No. DE-FG02-03ER15476. Computational research (including support for WA and PL) was carried out at Brookhaven National Laboratory under contract DE-SC0012704 with the US Department of Energy, Division of Chemical Sciences. DFT calculations were performed using computational resources at the Center for Functional Nanomaterials, Brookhaven National Laboratory under Contract No. DE-AC02-98CH10886, and at the National Energy Research Scientific Computing Center (NERSC), the latter of which is supported by the Office of Science of the U.S. DOE under Contract No. DE-AC02-05CH11231. Beamlines X18A and X19A at the NSLS were supported in part by the Synchrotron Catalysis Consortium, U. S. Department of Energy Grant No. DE-FG02-05ER15688. High-resolution electron microscopy data in this manuscript were collected in part at BNL's Center for Functional Nanomaterials, which is also supported by the U.S. Department of Energy under Contract No. DE-AC02-98CH10886 and DE-SC-00112704. RMC and RMA gratefully acknowledge support from the Chemical Sciences, Geosciences, and Biosciences Division, Office of Basic Energy Sciences, Office of Science, U. S. Department of Energy (Contract No. DE-FG02-13ER16428). Finally, we thank Dr. Nebojsa Marinkovic (NSLS II at BNL) for helpful discussions and advice.

6. Supporting Information Available

Additional structural characterization and electrochemical data of our samples are presented. This information is available free of charge via the Internet at http://pubs.acs.org/

References

(1) Morozan, A.; Jousselme, B.; Palacin, S. *Energ. Environ. Sci.* **2011**, *4*, 1238.

(2) Chen, Z. W.; Higgins, D.; Yu, A. P.; Zhang, L.; Zhang, J. J. *Energ. Environ. Sci.* **2011**, *4*, 3167.

(3) Stephens, I. E. L.; Bondarenko, A. S.; Gronbjerg, U.; Rossmeisl, J.; Chorkendorff, I. *Energ. Environ. Sci.* **2012**, *5*, 6744.

(4) Nilekar, A. U.; Xu, Y.; Zhang, J. L.; Vukmirovic, M. B.; Sasaki, K.; Adzic, R. R.; Mavrikakis, M. *Top. Catal.* **2007**, *46*, 276.

(5) Bing, Y. H.; Liu, H. S.; Zhang, L.; Ghosh, D.; Zhang, J. J. *Chem. Soc. Rev.* **2010**, *39*, 2184.

(6) Mazumder, V.; Lee, Y.; Sun, S. H. *Adv. Funct. Mater.* **2010**, *20*, 1224.

(7) Zhang, H.; Jin, M. S.; Xia, Y. N. *Chem. Soc. Rev.* **2012**, *41*, 8035.

(8) Wang, C.; Markovic, N. M.; Stamenkovic, V. R. *ACS Catal.* **2012**, *2*, 891.

(9) Oezaslan, M.; Hasche, F.; Strasser, P. *J. Phys. Chem. Lett.* **2013**, *4*, 3273.

(10) Guo, S. J.; Zhang, S.; Sun, S. H. *Angew. Chem. Int. Edit.* **2013**, *52*, 8526.

(11) Wu, J. B.; Yang, H. *Acc. Chem. Res.* **2013**, *46*, 1848.

(12) Xu, Y.; Zhang, B. *Chem. Soc. Rev.* **2014**, *43*, 2439.

(13) Xia, Y.; Yang, P.; Sun, Y.; Wu, Y.; Mayers, B.; Gates, G.; Yin, Y.; Kim, F.; Yan, H. *Adv. Mater.* **2003**, *15*, 353.

(14) Weber, J.; Singhal, R.; Zekri, S.; Kumar, A. *Int. Mater. Rev.* **2008**, *53*, 235.

(15) Wang, N.; Cai, Y.; Zhang, R. Q. *Mater. Sci. Eng. R* **2008**, *60*, 1.

(16) Cademartiri, L.; Ozin, G. A. *Adv. Mater.* **2009**, *21*, 1013.

(17) Lim, B.; Jiang, M.; Camargo, P. H. C.; Cho, E. C.; Tao, J.; Lu, X.; Zhu, Y.; Xia, Y. *Science* **2009**, *324*, 1302.

(18) Kitchin, J. R.; Norskov, J. K.; Barteau, M. A.; Chen, J. G. *Phys. Rev. Lett.* **2004**, *93*.

(19) Koenigsmann, C.; Zhou, W. P.; Adzic, R. R.; Sutter, E.; Wong, S. S. *Nano Lett.* **2010**, *10*, 2806.

(20) Koenigsmann, C.; Santulli, A. C.; Gong, K. P.; Vukmirovic, M. B.; Zhou, W. P.; Sutter, E.; Wong, S. S.; Adzic, R. R. *J. Am. Chem. Soc.* **2011**, *133*, 9783.

(21) Koenigsmann, C.; Sutter, E.; Adzic, R. R.; Wong, S. S. *J. Phys. Chem. C* **2012**, *116*, 15297.

(22) Koenigsmann, C.; Tan, Z.; Peng, H.; Sutter, E.; Jacobskind, J.; Wong, S. S. *Isr. J. Chem.* **2012**, *52*, 1090.

(23) Koenigsmann, C.; Scofield, M. E.; Liu, H. Q.; Wong, S. S. *J. Phys. Chem. Lett.* **2012**, *3*, 3385.

(24) Strasser, P.; Koh, S.; Anniyev, T.; Greeley, J.; More, K.; Yu, C. F.; Liu, Z. C.; Kaya, S.; Nordlund, D.; Ogasawara, H.; Toney, M. F.; Nilsson, A. *Nat. Chem.* **2010**, *2*, 454.

(25) Matanovic, I.; Kent, P. R. C.; Garzon, F. H.; Henson, N. J. *J. Electrochem. Soc.* **2013**, *160*, F548.

(26) Russell, A. E.; Tessier, B. C.; Wise, A. M.; Rose, A.; Price, S. W. T.; Richardson, P. W.; Ball, S. C.; Theobald, B.; Thompsett, D.; Crabb, E. M. *ECS Trans.* **2011**, *41*, 55.

(27) Rettew, R. E.; Allam, N. K.; Alamgir, F. M. *ACS Appl. Mater. Inter.* **2011**, *3*, 147.

(28) Cheon, J. Y.; Kim, T.; Choi, Y.; Jeong, H. Y.; Kim, M. G.; Sa, Y. J.; Kim, J.; Lee, Z.; Yang, T. H.; Kwon, K.; Terasaki, O.; Park, G. G.; Adzic, R. R.; Joo, S. H. *Sci. Rep.* **2013**, *3*, 2715.

(29) Gao, J.; Zhong, J.; Bai, L. L.; Liu, J. Y.; Zhao, G. Q.; Sun, X. H. *Sci Rep-Uk* **2014**, *4*, 3606.

(30) Nashner, M. S.; Frenkel, A. I.; Adler, D. L.; Shapley, J. R.; Nuzzo, R. G. *J. Am. Chem. Soc.* **1997**, *119*, 7760.

(31) Frenkel, A. I. *J. Synchrotron Radiat.* **1999**, *6*, 293.

(32) Frenkel, A. I.; Hills, C. W.; Nuzzo, R. G. *J. Phys. Chem. B* **2001**, *105*, 12689.

(33) Alayoglu, S.; Zavalij, P.; Eichhorn, B.; Wang, Q.; Frenkel, A. I.; Chupas, P. *ACS Nano* **2009**, *3*, 3127.

(34) Frenkel, A. I. *Chem. Soc. Rev.* **2012**, *41*, 8163.

(35) Jung, U.; Elsen, A.; Li, Y.; Smith, J. G.; Small, M. W.; Stach, E. A.; Frenkel, A. I.; Nuzzo, R. G. *ACS Catal.* **2015**, *5*, 1539.

(36) Dutta, I.; Carpenter, M. K.; Balogh, M. P.; Ziegelbauer, J. M.; Moylan, T. E.; Atwan, M. H.; Irish, N. P. *J. Phys. Chem. C* **2010**, *114*, 16309.

(37) Sasaki, K.; Naohara, H.; Choi, Y. M.; Cai, Y.; Chen, W. F.; Liu, P.; Adzic, R. R. *Nat. Commun.* **2012**, *3*, 1115.

(38) Kuttiyiel, K. A.; Sasaki, K.; Su, D.; Vukmirovic, M. B.; Marinkovic, N. S.; Adzic, R. R. *Electrochim. Acta* **2013**, *110*, 267.

(39) Anderson, R. M.; Zhang, L.; Loussaert, J. A.; Frenkel, A. I.; Henkelman, G.; Crooks, R. M. *ACS Nano* **2013**, *7*, 9345.

(40) Nashner, M. S.; Frenkel, A. I.; Somerville, D.; Hills, C. W.; Shapley, J. R.; Nuzzo, R. G. *J. Am. Chem. Soc.* **1998**, *120*, 8093.

(41) Knecht, M. R.; Weir, M. G.; Frenkel, A. I.; Crooks, R. M. *Chem. Mater.* **2007**, *20*, 1019.

(42) Shu, Y. Y.; Murillo, L. E.; Bosco, J. P.; Huang, W.; Frenkel, A. I.; Chen, J. G. *Appl. Catal. A* **2008**, *339*, 169.

(43) Teng, X. W.; Han, W. Q.; Wang, Q.; Li, L.; Frenkel, A. I.; Yang, J. C. *J. Phys. Chem. C* **2008**, *112*, 14696.

(44) Teng, X. W.; Wang, Q.; Liu, P.; Han, W.; Frenkel, A.; Wen, W.; Marinkovic, N.; Hanson, J. C.; Rodriguez, J. A. *J. Am. Chem. Soc.* **2008**, *130*, 1093.

(45) Kresse, G.; Furthmuller, J. *Phys. Rev. B* **1996**, *54*, 11169.

(46) Kresse, G.; Hafner, J. *Phys. Rev. B* **1993**, *47*, 558.

(47) Perdew, J. P.; Chevary, J. A.; Vosko, S. H.; Jackson, K. A.; Pederson, M. R.; Singh, D. J.; Fiolhais, C. *Phys. Rev. B* **1992**, *46*, 6671.

(48) Blochl, P. E. *Phys. Rev. B* **1994**, *50*, 17953.

(49) Monkhorst, H. J.; Pack, J. D. *Phys. Rev. B* **1976**, *13*, 5188.

(50) Koenigsmann, C.; Sutter, E.; Chiesa, T. A.; Adzic, R. R.; Wong, S. S. *Nano Lett.* **2012**, *12*, 2013.

(51) Norskov, J. K.; Rossmeisl, J.; Logadottir, A.; Lindqvist, L.; Kitchin, J. R.; Bligaard, T.; Jonsson, H. *J. Phys. Chem. B* **2004**, *108*, 17886.

(52) Stamenkovic, V.; Mun, B. S.; Mayrhofer, K. J. J.; Ross, P. N.; Markovic, N. M.; Rossmeisl, J.; Greeley, J.; Norskov, J. K. *Angew. Chem. Int. Edit.* **2006**, *45*, 2897.

(53) Shao, M.; Liu, P.; Adzic, R. R. *J. Phys. Chem. B* **2007**, *111*, 6772.

(54) Wang, J. X.; Inada, H.; Wu, L. J.; Zhu, Y. M.; Choi, Y. M.; Liu, P.; Zhou, W. P.; Adzic, R. R. *J. Am. Chem. Soc.* **2009**, *131*, 17298.

(55) Zhang, J.; Yang, H. Z.; Fang, J. Y.; Zou, S. Z. *Nano Lett.* **2010**, *10*, 638.

(56) An, W.; Liu, P. *J. Phys. Chem. C* **2013**, *117*, 16144.

(57) Weir, M. G.; Myers, V. S.; Frenkel, A. I.; Crooks, R. M. *ChemPhysChem* **2010**, *11*, 2942.

(58) Dowben, P.; Miller, A.; Vook, R. *Gold Bull.* **1987**, *20*, 54.

(59) Deng, L.; Hu, W. Y.; Deng, H. Q.; Xiao, S. F.; Tang, J. F. *J. Phys. Chem. C* **2011**, *115*, 11355.

(60) Zhang, Y.; Hsieh, Y. C.; Volkov, V.; Su, D.; An, W.; Si, R.; Zhu, Y. M.; Liu, P.; Wang, J. X.; Adzic, R. R. *ACS Catal* **2014**, *4*, 738.

(61) Carino, E. V.; Kim, H. Y.; Henkelman, G.; Crooks, R. M. *J. Am. Chem. Soc.* **2012**, *134*, 4153.

(62) Ramirez-Caballero, G. E.; Ma, Y. G.; Callejas-Tovar, R.; Balbuena, P. B. *Phys. Chem. Chem. Phys.* **2010**, *12*, 2209.

(63) Herron, J. A.; Mavrikakis, M. *Catal. Commun.* **2014**, *52*, 65.

(64) Hammer, B.; Norskov, J. K. *Nature* **1995**, *376*, 238.

(65) Rodriguez, P.; Garcia-Araez, N.; Koper, M. T. M. *Phys. Chem. Chem. Phys.* **2010**, *12*, 9373.

(66) Ruban, A. V.; Skriver, H. L. *Comp. Mater. Sci.* **1999**, *15*, 119.

(67) Ruban, A. V.; Skriver, H. L.; Norskov, J. K. *Phys. Rev. B* **1999**, *59*, 15990.

(68) Mavrikakis, M.; Hammer, B.; Nørskov, J. K. *Phys. Rev. Lett.* **1998**, *81*, 2819.

(69) Tripkovic, V.; Skúlason, E.; Siahrostami, S.; Nørskov, J. K.; Rossmeisl, J. *Electrochim. Acta* **2010**, *55*, 7975.

(70) Grgur, B. N.; Marković, N. M.; Ross, P. N. *Can. J. Chem.* **1997**, *75*, 1465.

(71) Antolini, E. *Energ Environ Sci* **2009**, *2*, 915.

(72) Xing, Y. C.; Cai, Y.; Vukmirovic, M. B.; Zhou, W. P.; Karan, H.; Wang, J. X.; Adzic, R. R. *J. Phys. Chem. Lett.* **2010**, *1*, 3238.

(73) Greeley, J.; Norskov, J. K. *Surf. Sci.* **2005**, *592*, 104.

(74) Adzic, R. R.; Zhang, J.; Sasaki, K.; Vukmirovic, M. B.; Shao, M.; Wang, J. X.; Nilekar, A. U.; Mavrikakis, M.; Valerio, J. A.; Uribe, F. *Top. Catal.* **2007**, *46*, 249.

(75) Kang, Y. J.; Snyder, J.; Chi, M. F.; Li, D. G.; More, K. L.; Markovic, N. M.; Stamenkovic, V. R. *Nano Lett.* **2014**, *14*, 6361.

(76) Mayrhofer, K. J. J.; Juhart, V.; Hartl, K.; Hanzlik, M.; Arenz, M. *Angew. Chem. Int. Edit.* **2009**, *48*, 3529.

(77) Volker, E.; Williams, F. J.; Calvo, E. J.; Jacob, T.; Schiffrin, D. J. *Phys. Chem. Chem. Phys.* **2012**, *14*, 7448.

(78) Jirkovsky, J. S.; Panas, I.; Romani, S.; Ahlberg, E.; Schiffrin, D. J. *J. Phys. Chem. Lett.* **2012**, *3*, 315.

(79) Kwon, G.; Ferguson, G. A.; Heard, C. J.; Tyo, E. C.; Yin, C. R.; DeBartolo, J.; Seifert, S.; Winans, R. E.; Kropf, A. J.; Greeley, J.; Johnston, R. L.; Curtiss, L. A.; Pellin, M. J.; Vajda, S. *ACS Nano* **2013**, *7*, 5808.

(80) Shao, M. H.; Huang, T.; Liu, P.; Zhang, J.; Sasaki, K.; Vukmirovic, M. B.; Adzic, R. R. *Langmuir* **2006**, *22*, 10409.

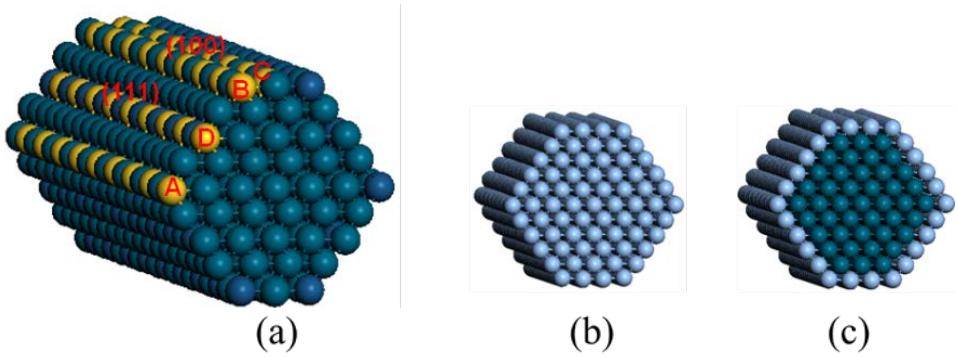

Figure 1. (a) Single Au atom sitting at various sites of a Pd NW. A: Edge (111)/(111); B: Edge (111)/(100); C: Terrace (100); D: Terrace (111); (b) Pt NW; and (c) Pd@Pt NW.

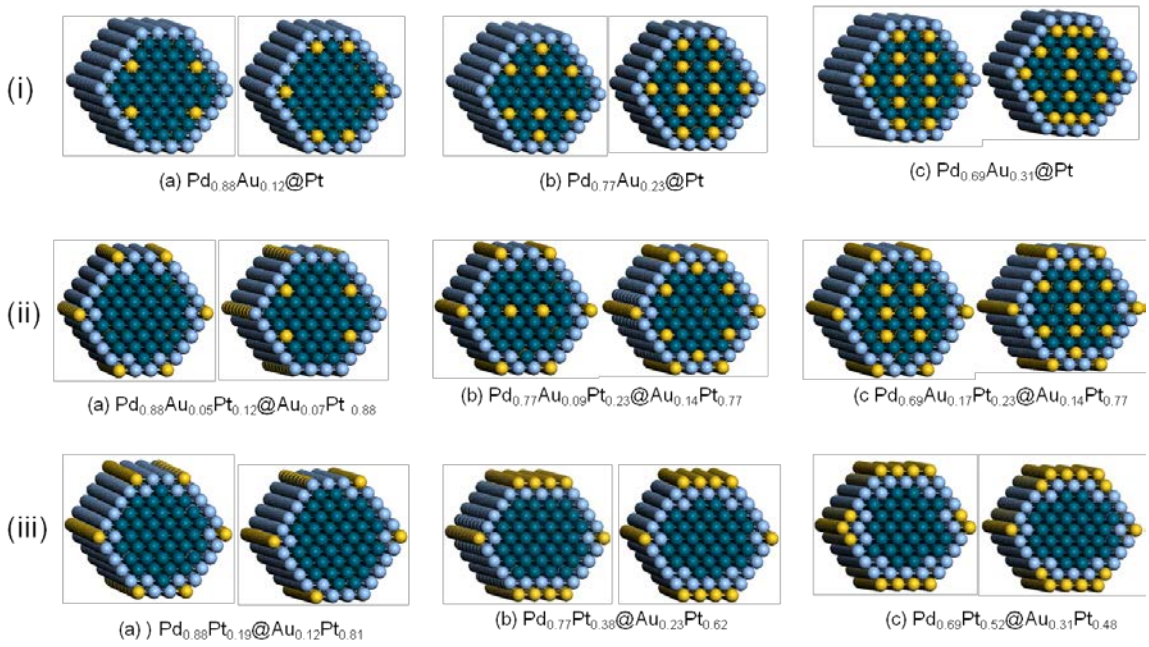

Figure 2. Hexagonal 2.2-nm-diameter $[(111)_4,(200)_2]$ nanowire models with various Au distributions. (a) Pd_9Au@Pt NWs, (b) Pd_8Au_2@Pt NWs, and (c) Pd_7Au_3@Pt NWs. Upper panel: (i) $Pd_{(1-x)}Au_x$@Pt NWs; Middle panel: (ii) $Pd_{(1-x)}Au_{(x-y)}Pt_z$@$Au_yPt_{(1-z)}$ NWs; Lower panel: (iii) $Pd_{(1-x)}Pt_z$@$Au_xPt_{(1-z)}$ NWs (see text). For clarity, eight supercells along the axis and bases at both ends were displayed.

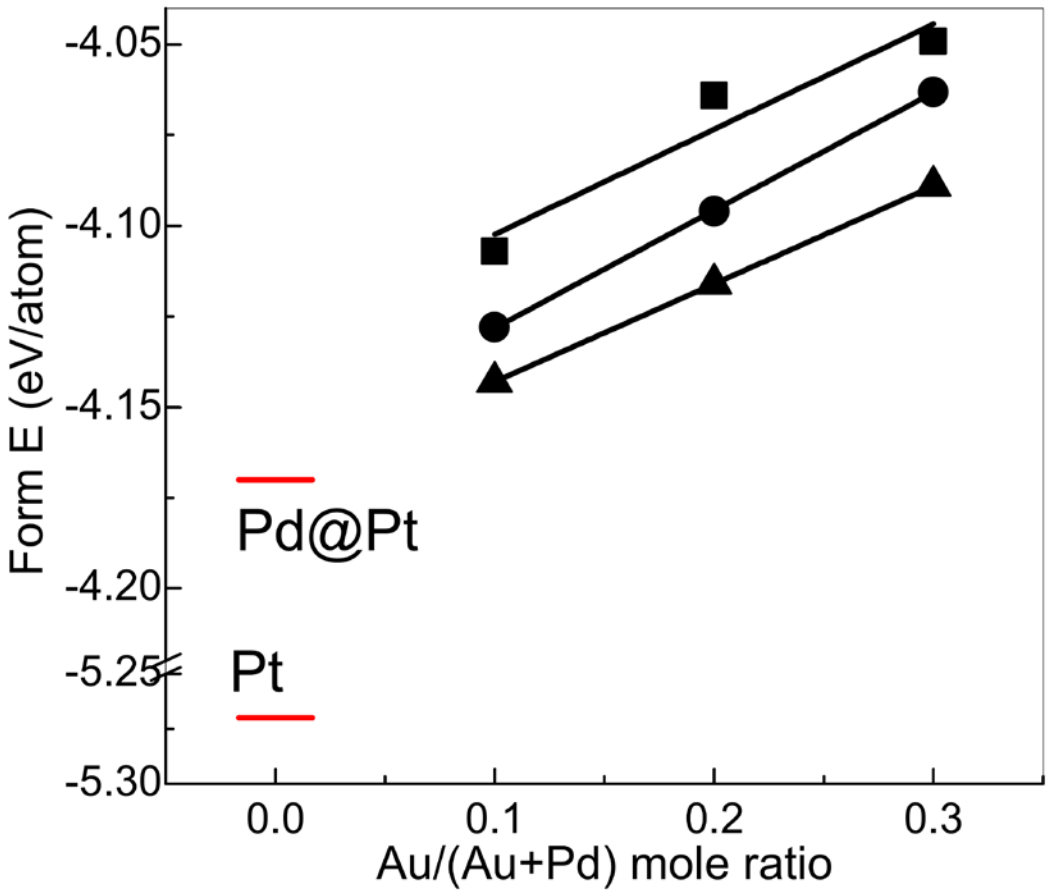

Figure 3. Formation energy of 2.2-nm-diameter NWs as a function of varying Au chemical compositions, as shown in Figure 2. Square: (i) $Pd_{(1-x)}Au_x$@Pt; Dot: (ii) $Pd_{(1-x)}Au_{(x-y)}Pt_z$@$Au_yPt_{(1-z)}$; Triangle: (iii) $Pd_{(1-x)}Pt_z$@$Au_xPt_{(1-z)}$. By means of comparison, pure Pt NWs and Pd@Pt NWs were also included.

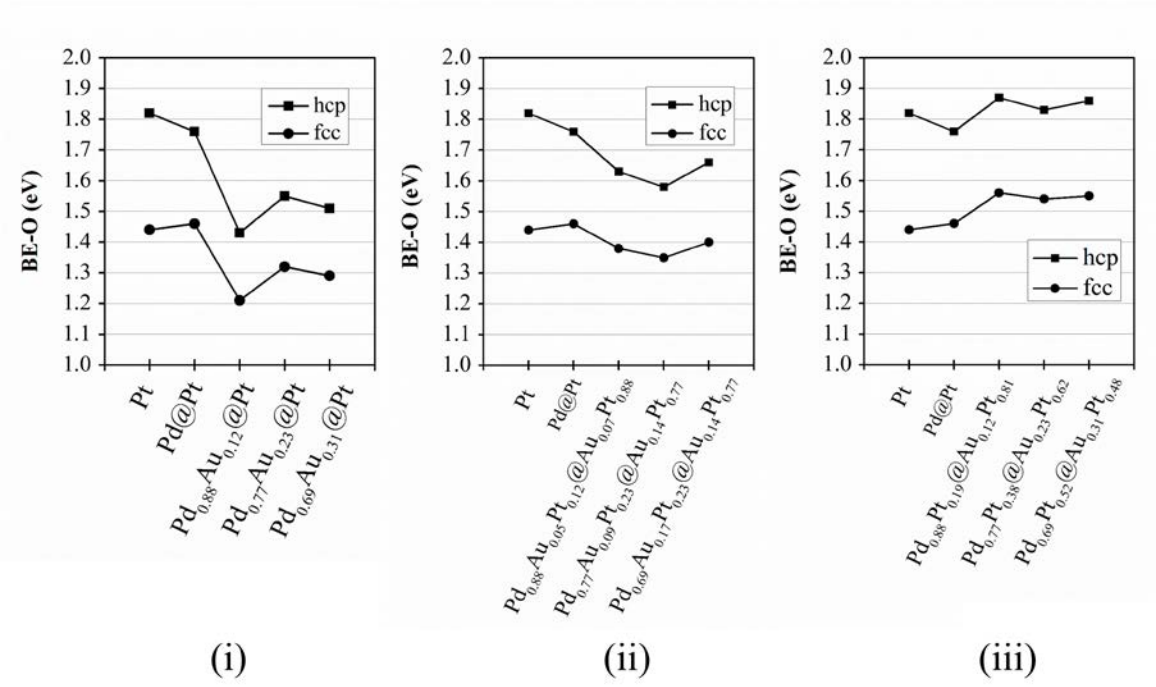

Figure 4. Calculated O-binding energy values at 3-fold hollow sites on Pt(111) terraces. (i) $Pd_{(1-x)}Au_x$@Pt NWs, (ii) $Pd_{(1-x)}Au_{(x-y)}Pt_z$@$Au_yPt_{(1-z)}$ NWs, and (iii) $Pd_{(1-x)}Pt_z$@$Au_xPt_{(1-z)}$ NWs.

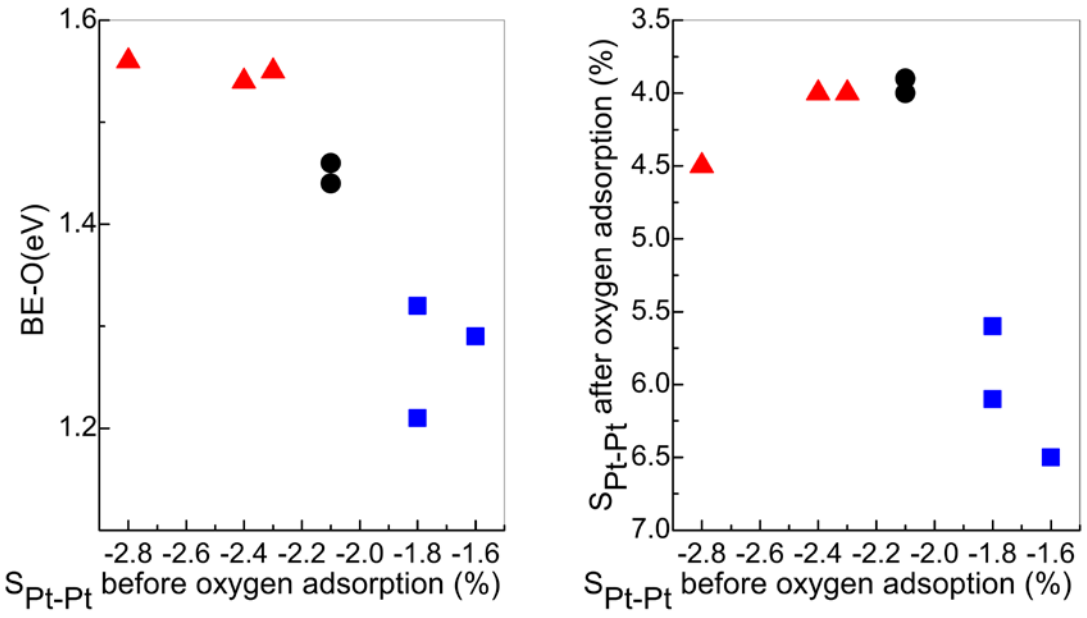

(a) (b)

Figure 5. (a) Calculated O-binding energy as a function of surface strain (S_{Pt-Pt}, only Pt-Pt bond length of the Pt triangle where O is bound was taken into account); (b) Surface strain (S_{Pt-Pt}) after O-binding as a function of surface contraction before O-binding; dot: Pt and Pd@Pt NWs; square: $Pd_{(1-x)}Au_x$@Pt NWs; triangle: $Pd_{(1-x)}Pt_z$@$Au_xPt_{(1-z)}$ NWs.

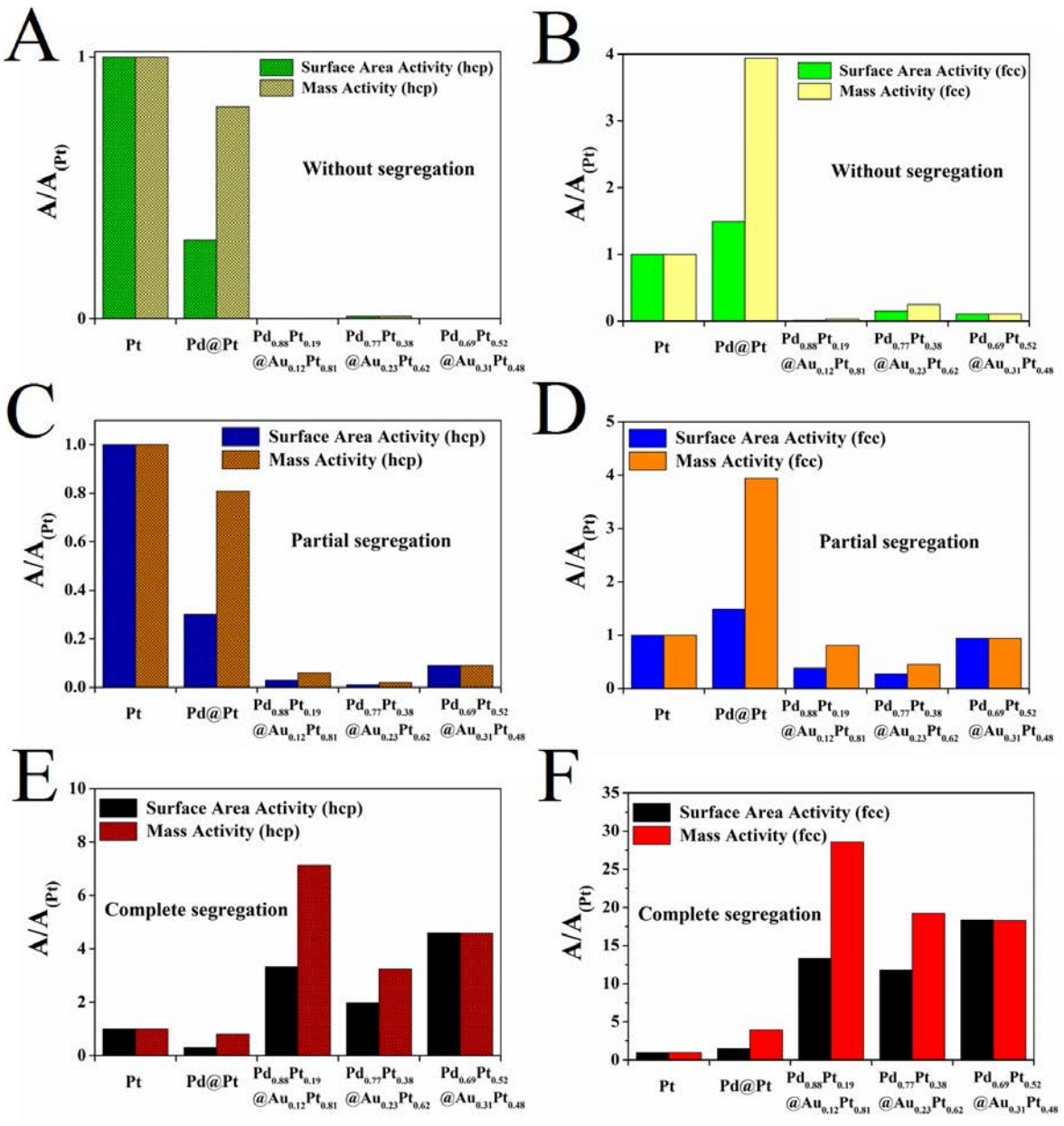

Figure 6. Estimated specific activity and mass activity for NWs at T = 20°C, based on the calculated BE-Os values. The top, uppermost two panels describe the predicted theoretical behavior of $Pd_{(1-x)}Au_x$@Pt NW systems, related with the *hcp* (A) and *fcc* (B) sites. Central, middle panels highlight the performance of $Pd_{(1-x)}Au_{(x-y)}Pt_z$@$Au_yPt_{(1-z)}$ NW systems, associated with the *hcp* (C) and *fcc* (D) sites. The bottom, lowermost panels designate $Pd_{(1-x)}Pt_z$@$Au_xPt_{(1-z)}$ NW systems, connected with the *hcp* (E) and *fcc* (F) sites.

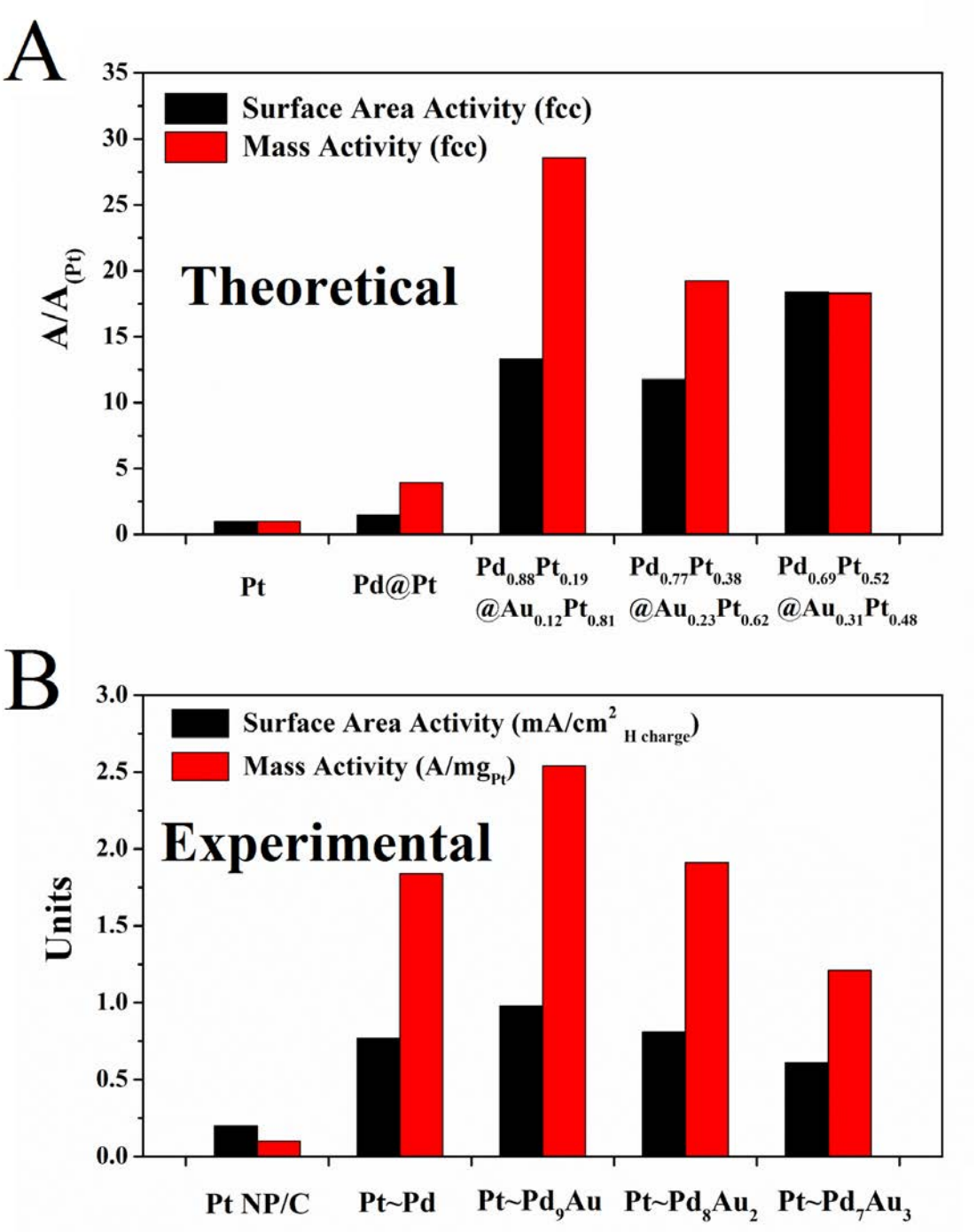

Figure 7. Comparison between (A) the theoretical estimated surface area activity (black) and mass activity (red) for different chemical compositions in a range of $Pd_{(1-x)}Pt_z@Au_xPt_{(1-z)}$ NWs, specifically on the *fcc* 3-fold sites, and (B) corresponding experimental results of ORR activities for a series of as-prepared $Pt\sim Pd_{1-x}Au_x$ nanowires. Data within Panel B are taken from *J. Phys. Chem. C*, **2012,** v.*116* (29), 15297-15306.

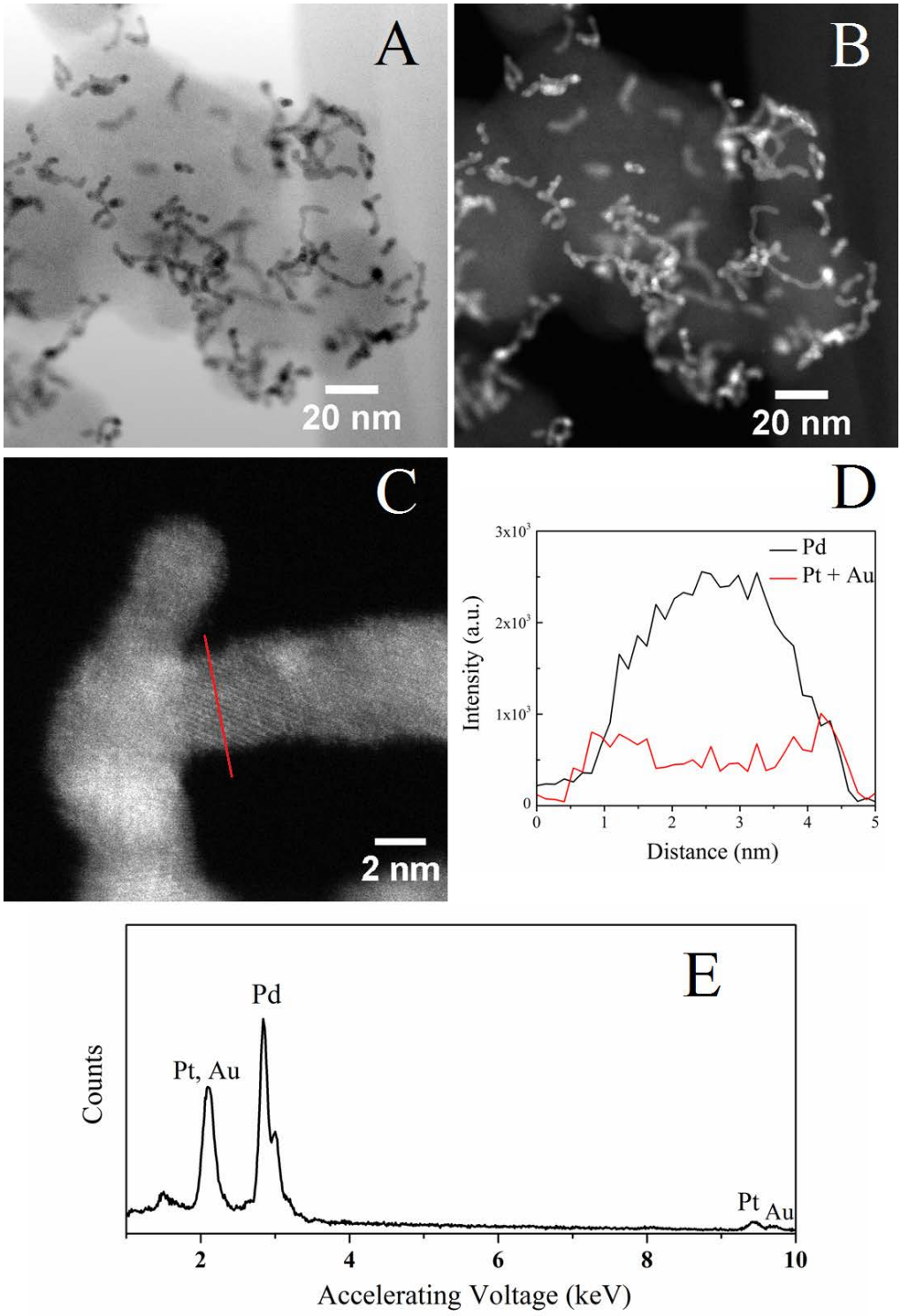

Figure 8. TEM results of as-synthesized Pt~Pd_9Au ultrathin nanowires. (A) Bright-field imaging, (B) high angle annular dark field imaging (HAADF), (C) high-resolution STEM imaging, (D) cross-sectional EELS analysis, and (E) representative EDS spectra are separately shown. The red line in panel C denotes the region where cross-sectional EELS has been taken.

Pt L_3 edge				
Sample	**Bond**	**N**	**R (Å)**	**σ^2 (Å^2)**
Freshly Made	Pt-Au/Pt	9.7 ± 1.1	2.705 ± 0.008	0.0089 ± 0.0009
Before reaction (0 cycle)		9.3 ± 0.9	2.699 ± 0.007	0.0089 ± 0.0009
After 10 cycles		8.6 ± 1.1	2.702 ± 0.009	0.0089 ± 0.0009
After 50 cycles		9.7 ± 1.0	2.710 ± 0.007	0.0089 ± 0.0009
After 250 cycles		9.3 ± 1.1	2.703 ± 0.009	0.0089 ± 0.0009
After 500 cycles		9.7 ± 1.1	2.703 ± 0.008	0.0089 ± 0.0009
After 750 cycles		9.9 ± 1.3	2.702 ± 0.010	0.0089 ± 0.0009
After 1000 cycles		9.4 ± 1.0	2.697 ± 0.007	0.0089 ± 0.0009

Table 1. Summary of structural parameters, including coordination number (N), bond length (R), as well as mean square disorder in bond length (σ^2) derived from fitting of the Pt L_3 edge spectra. The Pt-Au/Pt bonding pathway is primarily considered herein.

Au L_3 edge				
Sample	**Bond**	**N**	**R (Å)**	**σ^2 (Å^2)**
Freshly Made	Au- Au/Pt	6.0 ± 0.5	2.817 ± 0.003	0.0090 ± 0.0008
	Au-Pd	5.9 ± 0.3	2.782 ± 0.003	0.0100 ± 0.0005
Before reaction (0 cycle)	Au- Au/Pt	6.2 ± 0.6	2.817 ± 0.003	0.0090 ± 0.0008
	Au-Pd	5.8 ± 0.4	2.782 ± 0.003	0.0100 ± 0.0005
After 10 cycles	Au- Au/Pt	6.1 ± 0.5	2.817 ± 0.003	0.0090 ± 0.0008
	Au-Pd	6.0 ± 0.3	2.782 ± 0.003	0.0100 ± 0.0005
After 50 cycles	Au- Au/Pt	6.4 ± 0.6	2.817 ± 0.003	0.0090 ± 0.0008
	Au-Pd	5.7 ± 0.4	2.782 ± 0.003	0.0100 ± 0.0005
After 250 cycles	Au- Au/Pt	6.7 ± 0.6	2.817 ± 0.003	0.0090 ± 0.0008
	Au-Pd	5.7 ± 0.4	2.782 ± 0.003	0.0100 ± 0.0005
After 500 cycles	Au- Au/Pt	6.0 ± 0.5	2.817 ± 0.003	0.0090 ± 0.0008
	Au-Pd	5.9 ± 0.4	2.782 ± 0.003	0.0100 ± 0.0005
After 750 cycles	Au- Au/Pt	6.5 ± 0.6	2.817 ± 0.003	0.0090 ± 0.0008
	Au-Pd	5.8 ± 0.4	2.782 ± 0.003	0.0100 ± 0.0005
After 1000 cycles	Au- Au/Pt	6.7 ± 0.5	2.817 ± 0.003	0.0090 ± 0.0008
	Au-Pd	5.7 ± 0.3	2.782 ± 0.003	0.0100 ± 0.0005

Table 2. Summary of structural parameters including coordination number (N), bond length (R), as well as mean square disorder in bond length (σ^2) derived from fitting of the Au L_3 edge spectra. Both the Au-Au/Pt and Au-Pd bonding paths have been primarily taken into consideration herein.